ORIGINAL RESEARCH

Integrated Regional Cardiac Hemodynamic Imaging and RNA Sequencing Reveal Corresponding Heterogeneity of Ventricular Wall Shear Stress and Endocardial Transcriptome

Margaret E. McCormick, PhD; Elisabetta Manduchi, PhD; Walter R. T. Witschey, PhD; Robert C. Gorman, MD; Joseph H. Gorman, III, MD; Yi-Zhou Jiang, PhD; Christian J. Stoeckert, Jr, PhD; Alex J. Barker, PhD; Michael Markl, PhD; Peter F. Davies, PhD, ScD

***Background*—**Unlike arteries, in which regionally distinct hemodynamics are associated with phenotypic heterogeneity, the relationships between endocardial endothelial cell phenotype and intraventricular flow remain largely unexplored. We investigated regional differences in left ventricular wall shear stress and their association with endocardial endothelial cell gene expression.

***Methods and Results*—**Local wall shear stress was calculated from 4-dimensional flow magnetic resonance imaging in 3 distinct regions of human (n=8) and pig (n=5) left ventricle: base, adjacent to the outflow tract; midventricle; and apex. In both species, wall shear stress values were significantly lower in the apex and midventricle relative to the base; oscillatory shear index was elevated in the apex. RNA sequencing of the endocardial endothelial cell transcriptome in pig left ventricle (n=8) at a false discovery rate ≤10% identified 1051 genes differentially expressed between the base and the apex and 327 between the base and the midventricle; no differentially expressed genes were detected at this false discovery rate between the apex and the midventricle. Enrichment analyses identified apical upregulation of genes associated with translation initiation including mammalian target of rapamycin, and eukaryotic initiation factor 2 signaling. Genes of mitochondrial dysfunction and oxidative phosphorylation were also consistently upregulated in the left ventricular apex, as were tissue factor pathway inhibitor (mean 50-fold) and prostacyclin synthase (5-fold)—genes prominently associated with antithrombotic protection.

***Conclusions*—**We report the first spatiotemporal measurements of wall shear stress within the left ventricle and linked regional hemodynamics to heterogeneity in ventricular endothelial gene expression, most notably to translation initiation and anticoagulation properties in the left ventricular apex, in which oscillatory shear index is increased and wall shear stress is decreased. **(*J Am Heart Assoc*. 2016;5:e003170 doi: 10.1161/JAHA.115.003170)**

Key Words: 4-dimensional flow magnetic resonance imaging • endocardium • gene expression • hemodynamics • ventricle

Hemodynamic wall shear stress (WSS) occupies a central role in vascular biology, but its importance in cardiac physiology and pathology is less well understood. Endothelial cells (ECs) lining blood vessels sense and respond to shear stress by physiological adaptation or pathological change, resulting in site-specific phenotypes either tailored to the flow environment or promoting disease susceptibility. ECs, for example, in arterial regions of complex disturbed flow associated with distributing branch arteries and aortic curvature are primed for the formation of atherosclerotic lesions via chronic low-level activation of inflammatory and oxidative pathways.[1] There are few equivalent studies of endocardial EC (EEC) phenotypes despite important roles of EECs in regulating cardiac contractility through autocrine and paracrine signaling[2] and recognized differences between cardiac and vascular ECs that range from morphology to signaling molecule production (eg, prostacyclin[3]). The relationships between spatiotemporal hemodynamic characteristics and EEC phenotypes in the mature heart warrant more detailed investigation.

Recent studies in the developing heart indicate that embryonic EECs are responsive to shear stress.[4,5] These experiments relied primarily on basic (on–off) flow manipulations within the embryonic heart without consideration of

From the Institutes for Medicine and Engineering (M.E.M., Y.-Z.J., P.F.D.) and Biomedical Informatics (E.M., C.J.S.), Departments of Pathology and Laboratory Medicine (M.E.M., Y.-Z.J., P.F.D.), Radiology (W.R.T.W.), Surgery (R.C.G., J.H.G.), and Genetics (C.J.S.), Perelman School of Medicine, University of Pennsylvania, Philadelphia, PA; Departments of Radiology (A.J.B., M.M.) and Biomedical Engineering (M.M.), Northwestern University, Chicago, IL.

Accompanying Tables S1 through S5, Figures S1 through S3 and Video S1 are available at http://jaha.ahajournals.org/content/5/4/e003170/DC1/embed/inline-supplementary-material-1.pdf

Correspondence to: Peter F. Davies PhD, ScD, Department of Pathology & Laboratory Medicine, Perelman School of Medicine, University of Pennsylvania, 1010 Vagelos Building, 3340 Smith Walk, Philadelphia, PA 19104. E-mail: pfd@mail.med.upenn.edu

Received January 8, 2016; accepted February 19, 2016.

detailed hemodynamic characteristics. A study using primary cultures of adult EECs was restricted to the use of shear stress approximations of the left ventricular flow environment.[6] Recent advances in imaging, however, have made it possible to visualize, describe, and measure complex endocardial flow in vivo.[7]

Preservation of flow patterns throughout the left ventricle (LV) is important to maintain its efficient function.[8] The development of 4-dimensional (4D) flow magnetic resonance imaging (MRI), which relies on 3-dimensional (3D) velocity encoding concurrent with ECG gating, provides accurate spatial and temporal information about in vivo blood velocity throughout the cardiovascular system.[9] Intracardiac studies by Doppler imaging and 4D flow MRI demonstrate regional differences in both velocity and blood residence time within the LV.[10,11] Notably, slower velocities and longer residence time toward the apex of the heart suggest significant regional differences that we hypothesized would influence the WSS-induced endothelial phenotype, as reflected in the steady-state transcriptome profiles of regional EECs.

In this study, we calculated regional left ventricular WSS using 4D flow MRI in humans and pigs to show that WSS varies regionally throughout the LV of both species. We then isolated EECs from sites matched to the regional hemodynamic characteristics in pig LV and profiled gene expression by RNA sequencing (RNAseq) to demonstrate significant regional differences of EEC phenotypes.

Methods

4D Flow MRI Acquisition and Analysis

Measurement of intracardiac hemodynamics was performed using 4D flow MRI. An example of LV fluid dynamics obtained from these experiments is shown in Figure 1 and Video S1. These images demonstrate the complex hemodynamic patterns observed within the LV during the cardiac cycle. Specific details regarding 4D flow MRI acquisition in human and pigs follow.

Human MRI

MRI studies in volunteers were approved by the institutional review board, and informed consent was obtained from all participants. Cardiac imaging was performed on 8 healthy

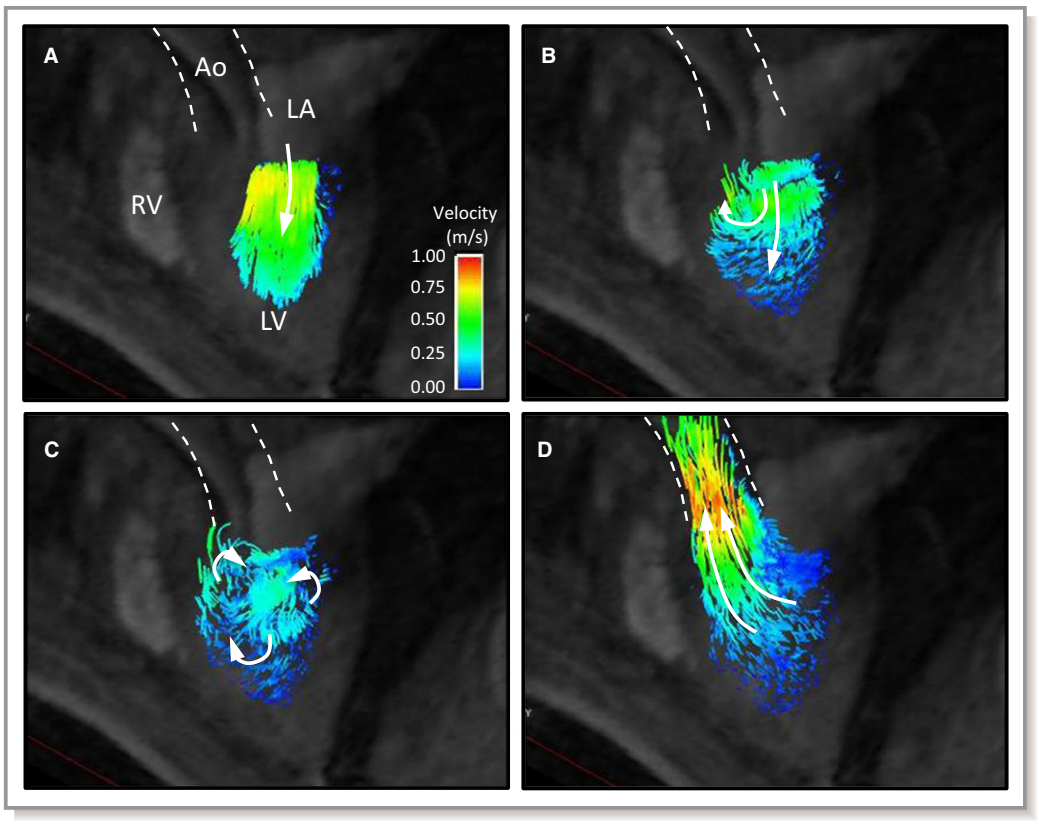

Figure 1. Pathline visualization of left ventricular flow dynamics. Four-chamber view of pig heart highlighting anatomical features of the heart including LV, LA, Ao, and RV. A, Early diastolic flow, (B) mid-diastole, (C) late diastole, (D) systole. Diastolic flow, when the mitral valve is open, is referred to as *inflow*. Systolic flow, when aortic valve is open, is referred to as *outflow*. Animations of hemodynamics in pig LV are provided in Video S1. Ao indicates aorta; LA, left atrium; LV, left ventricle; RV, right ventricle.

volunteers (mean age 24±1.8 years; 4 female and 4 male) (Table S1). All data were acquired on a 3-T MRI system (Trio; Siemens). Prospectively ECG-gated time-resolved 3D phase-contrast MRI with 3-directional velocity encoding (4D flow MRI) was used to measure in vivo 3D blood flow velocity with full volumetric coverage of the LV. The 4D flow MRI data were acquired during free breathing using navigator gating of the diaphragm motion.[12] Further 4D flow MRI pulse sequence parameters were as follows: flip angle 7°, spatial resolution 2.5×2.9×3.0 mm, temporal resolution 38.4 ms, imaging acceleration using the Generalized Autocalibrating Partially Parallel Acquisitions (GRAPPA) technique with a reduction factor of R=2, total acquisition time of 10 to 15 minutes depending on heart rate and navigator efficiency, velocity sensitivity 150 cm/s.

Pig MRI

Animal experiments were performed in compliance with the Guide for the Care and Use of Laboratory Animals (National Institutes of Health publication 85-23, revised 1996) and approved by the University of Pennsylvania Institutional Animal Care and Use Committee. Healthy adult pigs (n=5, Yorkshire swine, weight 61.6±2.9 kg; range 59–67 kg) were sedated and intubated, and anesthesia was maintained with a mixture of isoflurane (1–2%) and oxygen throughout the procedure. Central arterial access was obtained surgically through the left carotid artery for LV blood pressure monitoring (Millar Instruments). MRI was performed on a 3-T whole-body MRI (Tim Trio model; Siemens Healthcare) using a prospective, 3D phase-contrast MRI sequence. Images were acquired with spatial resolution 2×2×2 mm^3, temporal resolution 20.8 ms, echo time 2.7 ms, field of view 320×320 mm^2, and bandwidth 460 Hz/pixel.

Data processing and WSS analysis

An overview of data processing and WSS analysis of both human and pig is shown in Figure 2 and was performed as described previously.[13] Local WSS and oscillatory shear indices (OSIs) were calculated in 3 distinct regions of the LV: base, inferior to the aortic valve on the posterior heart wall; midventricle (midV), inferior to the mitral valve on the free wall; and the LV apex. As shown in Figure 2A, 2-dimensional planes through the LV were selected at the base, midV and apex using EnSight 10.0 (CEI; Apex). Following plane selection, the planes were manually segmented in all time frames to define the LV lumen (Figure 2B). This was achieved by adjusting the position of a set number of points

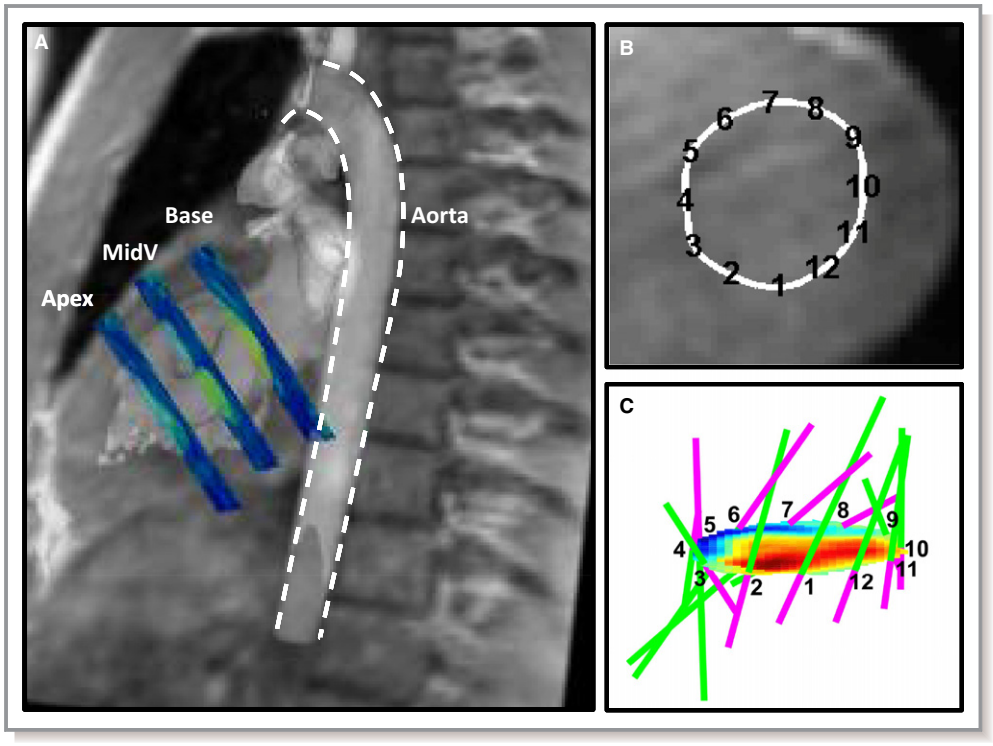

Figure 2. Methodology for magnetic resonance imaging analysis. A, Example of 2D plane selection from the 3 regions (base, midV, and apex) through the human LV. Planes are color-coded for velocity. The aorta is outlined and labeled for reference. B, Example of manual segmentation of the LV lumen from a 2D plane. C, Intraventricular blood flow velocities (color scale red to blue); lines show wall shear stress magnitude and direction (green) and oscillatory shear index (purple) magnitude. 2D indicates 2-dimensional; LV, left ventricle; midV, midventricle.

(shown in Figure 2B). After segmentation, endocardial WSS was calculated using velocity gradients found along the segmentation contour.[13] A representative result is shown in Figure 2C (colors indicate intraventricular blood flow velocities; green lines indicate WSS magnitude and direction, whereas purple lines show OSI magnitude). Specific points along the segmented lumen were matched to regions of EEC isolation (pig) for each heart region: base, points 4 to 7; midV, points 9 to 11; apex, all 12 points. WSS was averaged across these points and then plotted against time.

Sources of potential error, including Maxwell terms, eddy currents, and velocity aliasing, were corrected during data processing.[13] Because manual segmentation can introduce error into WSS calculations, 2 independent observers segmented the LV lumen for both human and pig with concordant results (Table S2).

WSS alignment

To account for differences in timing and duration of cardiac phases between individual hearts and between species, WSS data were normalized to the cardiac cycle using MATLAB software (Mathworks). Normalization was based on diastole (inflow) as ≈60% and systole ≈40% (outflow) of the cardiac cycle (Figure 3).

EEC Sampling and RNAseq

EECs were isolated from an additional 8 pigs. Briefly, a transverse incision was made 5 mm from the apex of the heart to reveal the apical lining of ECs, and a longitudinal incision was made 0.5 to 1 cm left of the left anterior descending artery through the anterior free wall to expose the main LV chamber. Following an ice-cold buffered saline rinse, 1 to 2 cm^2 of endothelium was gently scraped from each region (Figure 5) and placed in mirVana RNA isolation buffer (Ambion; ThermoFisher). Nucleic acid isolation, purification, quality control, and concentration were performed, as described previously.[14]

RNA library preparation and sequencing

RNA samples from 3 regions (base, midV, apex) in 8 male pigs (24 total samples) were submitted for sequencing (RNAseq) to

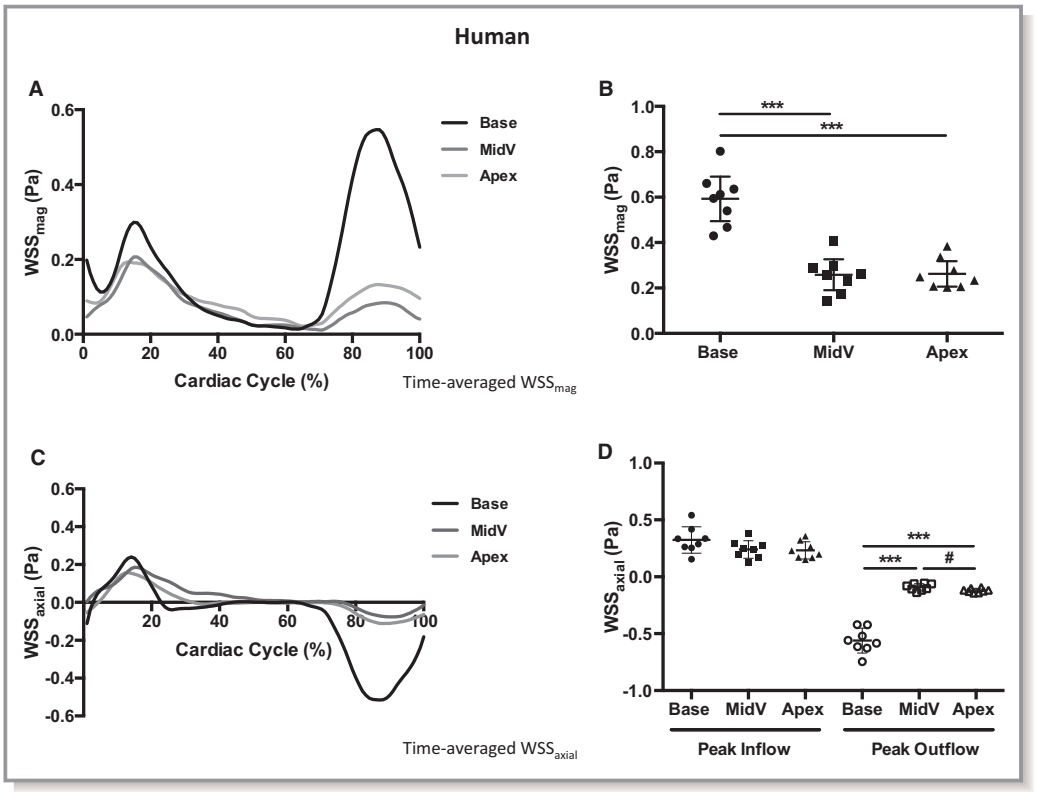

Figure 3. The 4-dimensional flow magnetic resonance imaging analysis of human endocardial WSS_{mag} and WSS_{axial}. A, Average WSS_{mag} (in Pa) during the cardiac cycle for the base, midV, and apex in healthy human hearts. B, Quantitation of peak WSS_{mag}. Data represent mean±SD (n=8, ***P<0.005). C, Average WSS_{axial} during the cardiac cycle for base, midV, and apex. D, Quantitation of average peak inflow (diastole, first 60% cardiac cycle) and peak outflow (systole, second 40% cardiac cycle) in the 3 regions of interest. Data represent mean±SD (n=8, ***P<0.005, #P<0.05). MidV indicates midventricle; WSS_{axial}, axial wall shear stress; WSS_{mag}, wall shear stress magnitude.

the Children's Hospital of Philadelphia High-Throughput Sequencing Center for quality control, library construction, and sequencing. Extracted RNA samples underwent quality control (Agilent Bioanalyzer); RNA integrity number and RNA concentration were measured. Following preparation (TruSeq RNA Sample Preparation Kit, version II; Illumina), the libraries were sequenced using the Illumina HiSeq 2500 with 100 base pair paired-end reads and yielded an average of about 32 million read pairs per sample.

Preprocessing and differential gene expression analysis

Reads were aligned to the Sscrofa10.2.73 genome with STAR.[15] The PORT pipeline (https://github.com/itmat/Normalization) was used for normalization and quantification. Two approaches were used for differential expression (with comparisons run in paired-by-pig mode): edgeR[16] and PADE (https://github.com/itmat/pade), an extension of PaGE.[17] For each comparison, we took the genes identified by both approaches at the desired false discovery rate. As an additional filter, genes with average normalized counts <50 in each of the 2 regions compared were excluded from analysis.

Pathway analysis

Data were analyzed by Qiagen Ingenuity Pathway Analysis software (IPA; Qiagen). We selected a false discovery rate of 0.10 (10%) for gene list analysis. Gene ontology enrichment analysis (GO Biological Process and Molecular Function) was performed using the Database for Annotation, Visualization and Integrated Discovery (DAVID) Web server (http://david.abcc.ncifcrf.gov/).[18,19] Identified canonical pathways were ranked according to *P* value.

Quantitative polymerase chain reaction (qPCR), Western blotting, and immunofluorescence procedures were performed as described previously.[14] Primers used for qPCR are shown in Table S5.

Accessibility of Data

The RNAseq data and metadata have been deposited into the ArrayExpress public repository (https://www.ebi.ac.uk/arrayexpress/) with accession number E-MTAB-3669.

Statistical Analysis of MRI and qPCR Data

Data are shown as mean±SD unless otherwise specified. Group comparisons were performed using ANOVA with Bonferroni correction for multiple comparisons. An adjusted *P* value of <0.05 was considered statistically significant. Statistical analysis was performed using GraphPad Prism 6 (GraphPad Software).

A Note on RNAseq Replicates

A sample size of 8 for biological replicates is at the upper end of what is typical in the RNAseq field. Power calculations are of little direct value in determining animal numbers for high-throughput experiments, including sequencing experiments. In RNAseq, thousands of genes at a time are analyzed with different expression distributions. Moreover, multiple testing corrections are needed. We used 2 different analysis methods (edgeR and PaGE/PADE) that have been developed specifically for this type of high-throughput data (and accounting for multiple testing). Leaning to the conservative side, we focused on the genes identified by both methods. Each of these methods of analysis was run in paired mode (pairing by pig), as indicated.

Results

Regional Differences in LV WSS and OSI

In both healthy adult humans and adult swine, the WSS magnitude and its 2 components axial and circumferential WSS were calculated. The axial WSS is of particular interest

Table 1. Regionally Averaged Human Left Ventricle WSS and OSI in Human

	WSS (Pa)			OSI (%)		
	Magnitude	Axial	Circumferential	3D	Axial	Circumferential
Base	Max: 0.59±0.11	Peak inflow: 0.32±0.11	Max: 0.16±0.08	23.4±6.4	23.9±7.3	23.4±6.4
		Peak outflow: −0.56±0.11	Min: −0.09±0.02			
MidV	Max: 0.26±0.08***	Peak inflow: 0.24±0.07	Max: 0.08±0.03*	27.4±6.2	26.8±5.9	25.8±8.7
		Peak outflow: −0.09±0.03***	Min: −0.05±0.03			
Apex	Max: 0.26±0.06***	Peak inflow: 0.23±0.08	Max: 0.04±0.01 ***,##	31.0±4.2*,#	32.1±5.0*,##	27.2±4.0
		Peak outflow: −0.12±0.02***,#	Min: −0.02±0.008***,#			

3D indicates 3-dimensional; max, maximum; midV, midventricle; min, minimum; OSI, oscillatory shear index; WSS, wall shear stress.
To base *P<0.05, ***P<0.005.
To MidV #P<0.05, ##P<0.01.

because it indicates the predominant direction of WSS along the long axis of the ventricle throughout the cardiac cycle.

Human

Analyses of 4D flow MRI in human LV revealed distinct regional patterns of WSS (Figure 3, Table 1). The age, heart rate, and left ventricular ejection fractions of the individual participants are shown in Table S1. Time-averaged WSS magnitude (Figure 3A and 3B) was significantly higher in the LV base (0.59 Pa) relative to midV and apex (both 0.26 Pa) (Table 1). Furthermore, time-averaged axial WSS (Figure 3C and 3D) demonstrated that these differences primarily occurred during outflow (systole); we did not observe any significant differences in axial WSS during peak inflow between regions. WSS data for individual participants are shown in Figure S1. WSS values fell within the range observed in the aorta throughout the cardiac cycle.[13]

In addition to WSS, the 3D, axial, and circumferential OSIs demonstrated regional heterogeneity (Table 1). OSI provides an indicator of oscillatory WSS and allows for quantification of the change in direction and magnitude of WSS. Although OSI was significant throughout the LV, the apex recorded significantly higher 3D and axial OSI than the base and midV (Table 1). High OSI in arteries is frequently associated with vascular pathologies.[20,21]

Pig

The 4D flow MRI data in pigs (Figure 4, Table 2) were qualitatively similar to those of humans. Time-averaged WSS magnitude and axial WSS were both reduced in the pig midV and apex (versus base), principally during outflow. Of note, the OSI differentials in the pig apex and midV versus base were greater than those in the human LV, particularly 3D and axial OSI (Table 2), and circumferential OSI was increased to significance ($P<0.05$). Although peak values of WSS and OSI were attenuated in pig LV compared with human, the overall trends were similar. Data from individual pigs are shown in Figure S2.

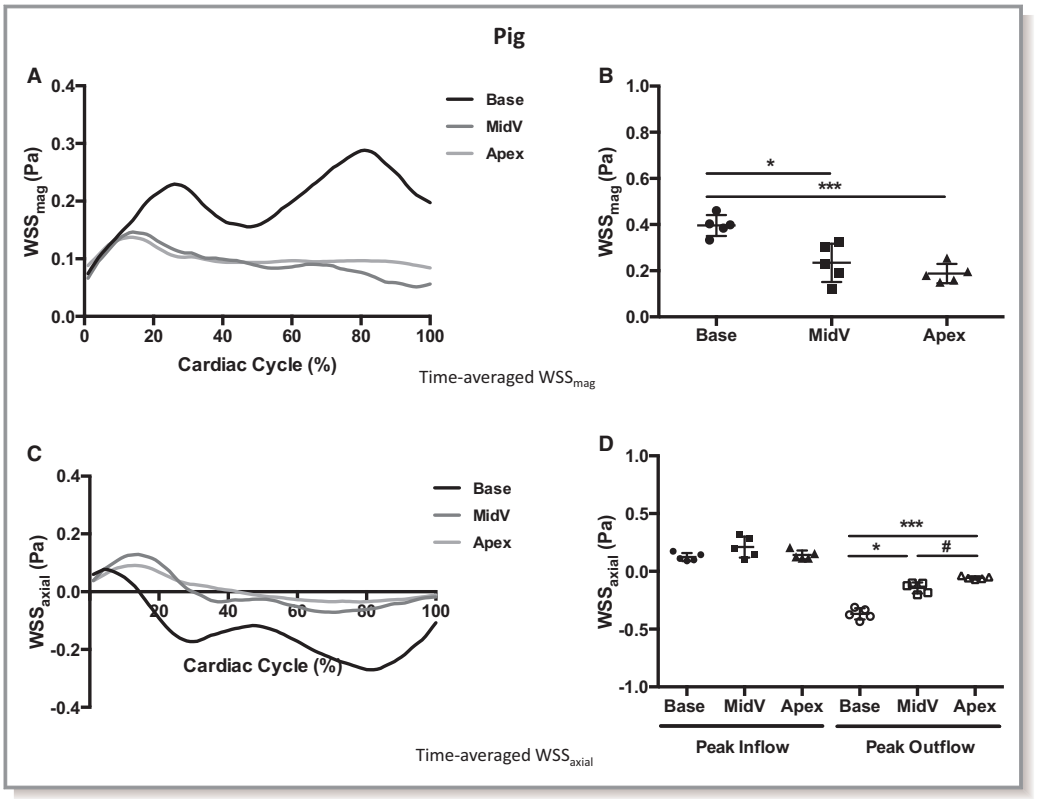

Figure 4. The 4-dimensional flow magnetic resonance imaging analysis of pig endocardial WSS_{mag} and WSS_{axial}. A, Average WSS_{mag} (in Pa) during the cardiac cycle for the base, midV, and apex in pig hearts. B, Quantitation of peak WSS_{mag}. Data represent mean±SD (n=5, $^{*}P<0.05$, $^{***}P<0.005$). C, Average WSS_{axial} during the cardiac cycle for base, midV, and apex. D, Quantitation of average peak inflow (diastole, first 60% cardiac cycle) and peak outflow (systole, second 40% cardiac cycle) in the 3 regions of interest. Data represent mean±SD (n=5, $^{*}P<0.05$, $^{***}P<0.005$, $^{\#}P<0.05$). MidV indicates midventricle; WSS_{axial}, axial wall shear stress; WSS_{mag}, wall shear stress magnitude.

Table 2. Regionally Averaged Left Ventricle WSS and OSI in Pig

	WSS (Pa)			OSI (%)		
	Magnitude	Axial	Circumferential	3D	Axial	Circumferential
Base	Max: 0.39±0.04	Peak inflow: 0.12±0.04	Max: 0.07±0.05	11.8±4.1	9.35±5.0	21.6±5.6
		Peak outflow: −0.36±0.05	Min: −0.13±0.06			
MidV	Max: 0.23±0.08*	Peak inflow: 0.21±0.09	Max: 0.07±0.03	30.2±7.8**	31.6±10.9**	31.1±9.5
		Peak outflow: −0.14±0.05**	Min: −0.04±0.01*			
Apex	Max 0.19±0.04***	Peak inflow: 0.14±0.04	Max: 0.04±0.02#	31.3±2.1***	31.7±3.0***	29.7±2.4*
		Peak outflow: −0.06±0.01 ***,#	Min: −0.03±0.005*			

3D indicates 3-dimensional; max, maximum; midV, midventricle; min, minimum; OSI, oscillatory shear index; WSS, wall shear stress.
To base *P<0.05, **P<0.01, ***P<0.005.
To MidV #P<0.05.

Transcriptome Analysis Identifies Broad Differences in Gene Expression Between Endocardial Regions

Encouraged by the similarity in regional WSS between LV regions in human and pig, we investigated phenotype differences of pig EECs in the 3 regions (Figure 5A and 5C). Sample selection was spatially matched to locations evaluated by 4D flow measurements. Pure populations of ECs were confirmed by Western blot (Figure 5B) and immunofluorescence staining (Figure 5D). Importantly, these samples were negative for the cardiomyocyte marker troponin.

RNAseq of pig EECs from base, midV, and apex was performed in 8 animals, in 3 regions per animal. Multidimensional scaling analysis, allows visualization of data set similarity and explores regional separation of the samples. In a multidimensional scaling plot (Figure 6A), each point represents 1 sample, and the distance between 2 points reflects the leading log fold-change of the corresponding RNA samples. The leading log fold-change is the average (root mean square) of the 500 largest absolute log fold-changes for genes between those 2 samples. The greatest separation was observed between apex and base (shown in blue and green, respectively, in Figure 6A).

For RNAseq analysis, a false discovery rate ≤0.10 was used in the following comparisons: base:apex, base:midV, and apex:midV. The base:apex comparison identified 1051 differentially expressed genes (DEGs), whereas 325 genes were differentially expressed between base and midV (Figure 6B). No significant DEGs were identified between midV and apex (false discovery rate 0.10). This result enforces phenotypic similarity between apex and midV and correlates with comparable values of WSS observed in these regions. In Figure 6C, a heat map of DEGs, clustered by gene and grouped by region, indicates similarity in gene expression among apex and midV regions and further illustrates their differences compared with the base. Hierarchical clustering of regions from individual animals is shown in Figure S3. Validation of a selection of DEGs by plotting their expression levels by qPCR against RNAseq values showed a robust correlation (R^2=0.84) (Figure 6D).

Pathway Analysis of RNAseq Data

IPA and DAVID[18,19] were applied to assess changes in biological or signaling pathways associated with gene expression (Tables S3 and S4, respectively). Initial analysis focused on the comparisons between base:apex and base:midV, in which the greatest WSS differences occurred. Both IPA and DAVID ranked translational pathways at the top of the list including eukaryotic initiation factor 2 (eIF2) and mammalian target of rapamycin (mTOR) signaling, translation elongation, and regulation of cell growth.

MRI analysis in both species established the largest differences in WSS between the base and the apex; therefore, we restricted pathway analysis to the 833 DEGs specific to this comparison (Figure 6B). The top 3 canonical pathways identified were eIF2 signaling, mTOR signaling, and regulation of eIF4 and p70S6K signaling. Because these pathways are represented when DEGs are restricted to the base:apex comparison, it suggests apical specificity. IPA further identified mitochondrial dysfunction and oxidative phosphorylation, which are unique to the restricted comparison (Table 3).

Despite classification as 3 separate pathways, eIF2, mTOR, and eIF4/p70S6K are all elements of the broader translation machinery, with a focus on translation initiation. Notably, of the 55 unique genes represented among these pathways, there was a large degree of overlap (Figure 7A). Furthermore, of the 55 DEGs, 50 were upregulated in the apex, including members of the 60s (large) and 40s (small) ribosomal subunits and several eukaryotic initiation factors. Figure 7B provides an overview of translational initiation and highlights parts of the pathway that are upregulated (in green) in the apex. Enhanced expression of components required for

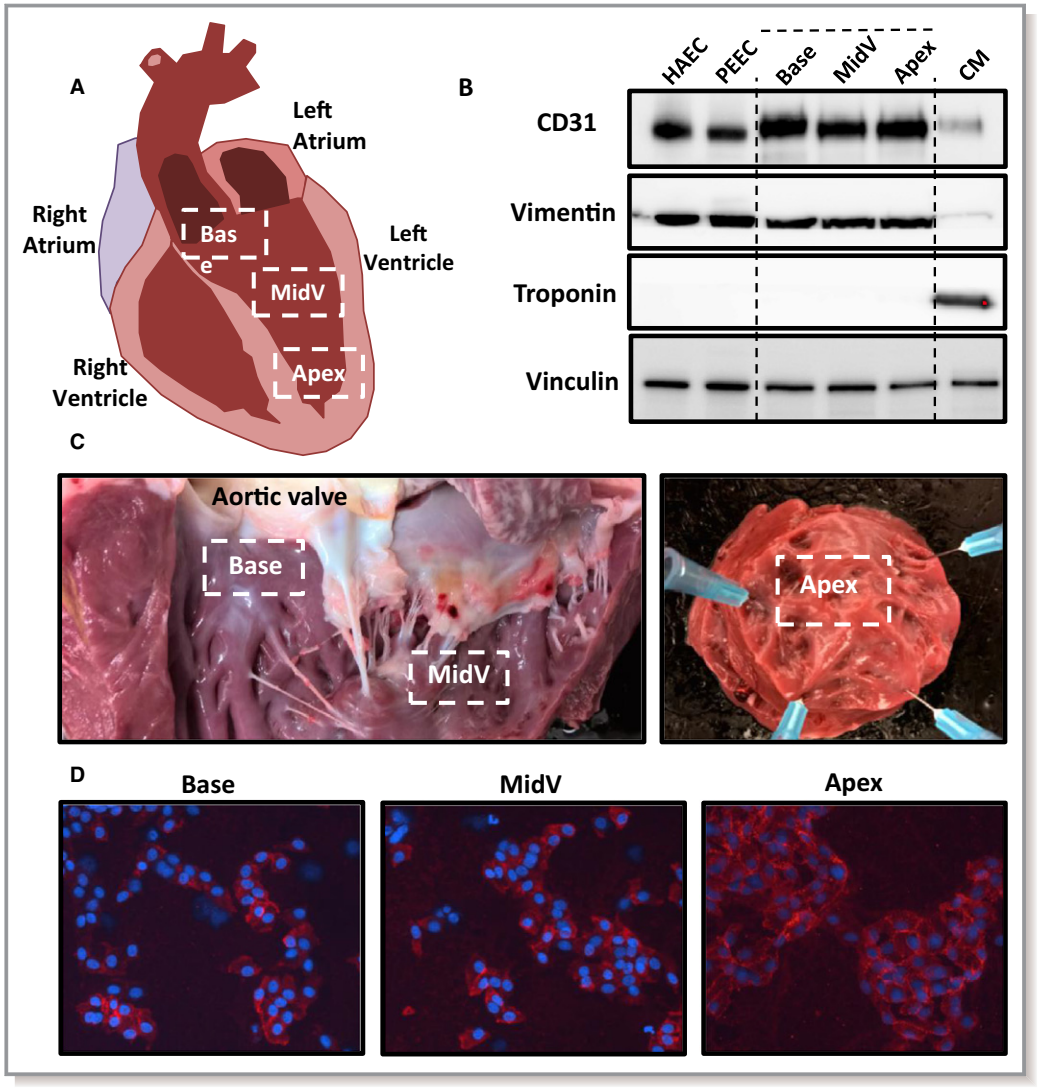

Figure 5. Endocardial regions of RNA and tissue isolation. A, Locations of LV regions. B, Representative Western blot (n=5) of isolated regional endocardial cells stained with identity markers CD31 (PECAM1), vimentin and troponin; vinculin was used for loading. C, Gross images of regions of LV regions. D, Isolated endocardial endothelial cell purity assessed by immunofluorescence staining for the endothelial marker PECAM1/CD31 (red) and nuclear stain DAPI (blue). CM indicates pig cardiomyocyte; HAEC, human aortic endothelial cell; LV, left ventricle; midV, midventricle; PEEC, pig endocardial endothelial cell.

translational initiation suggests that rates of translation may be elevated in the apex relative to the base. An exception is the reduced expression of PERK/EIF2AK3 (shown in red in Figure 7B), the function of which is inhibition of translation initiation; therefore, its reduced expression further supports increased translational activity. Although the mechanisms driving elevated expression of translation-focused genes in EECs from the LV apex are unclear, previous studies have demonstrated that WSS is able to regulate endothelial translation and activate mTOR signaling.[22] Importantly, mTOR integrates environmental cues to function as a master regulator of translation.

Similar to the translation-focused pathways, there was considerable overlap among genes present in the mitochondrial dysfunction and oxidative phosphorylation pathways. IPA identified 21 unique genes between these 2 pathways, with the majority of genes represented by oxidative phosphorylation (Figure 7C). Importantly, all of the genes identified were upregulated in the apex; in particular, the 14 common genes were found to be components of mitochondrial complexes I to V, which are involved in electron transport and ATP synthesis (Figure 7D). This suggests a possible difference in metabolic activity between base and apex. Despite increased expression of mitochondrial genes, mitochondrial DNA content did not differ between base and apex EECs (data not shown).

Evidence from the restricted IPA suggests that protein translation and oxidative phosphorylation pathways are upregulated in the apex compared with the base (Table 3).

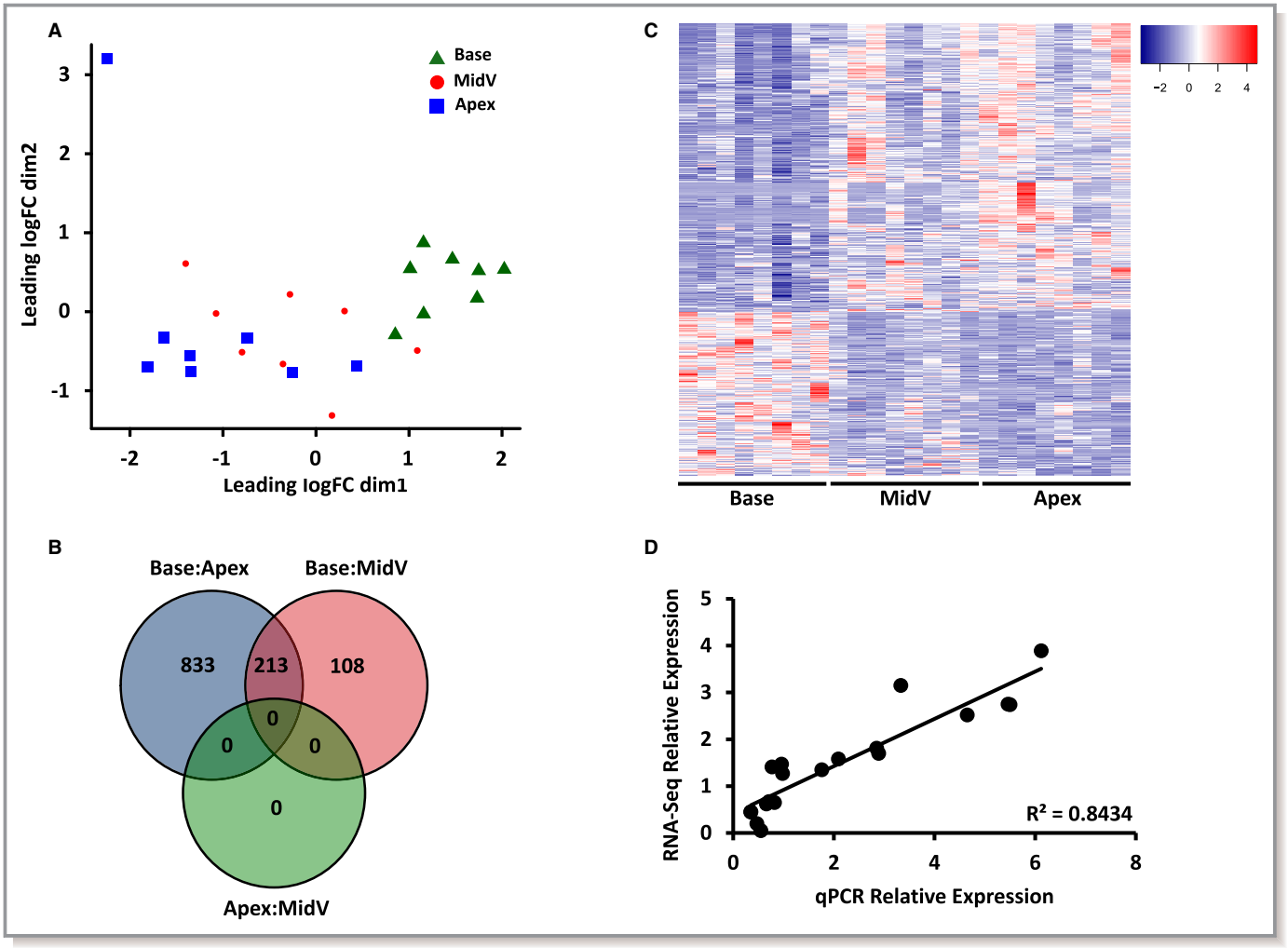

Figure 6. RNAseq data analysis. A, Multidimensional scaling plot generated with edgeR (green: base; red: midV; blue: apex). Each point represents 1 sample, and the distance between 2 points reflects the leading logFC of the corresponding RNA samples. The leading logFC is the average (root mean square) of the 500 largest absolute logFCs for genes between those 2 samples. B, Heat map of the union of the DEGs from (A) at FDR 0.10 (red: upregulated; blue: downregulated). Rows (genes) have been clustered, columns (samples) are displayed grouped by condition. C, Venn diagram showing numbers of DEGs (FDR 0.10) in comparisons of base:apex, base:midV, and apex:midV. D, Scatterplot of RNAseq (*y*-axis) vs qPCR data (*x*-axis) using relative expression of base:apex, n=19 genes, R^2=0.84342. DEG indicates differentially expressed gene; dim, dimension; FDR, false discovery rate; logFC, log fold-change; midV, midventricle; qPCR, quantitative polymerase chain reaction; RNAseq, RNA sequencing.

A possibility is that the energy requirement for translation results in elevated oxidative phosphorylation linked to upregulation of the associated genes.

Upregulation of Antithrombosis Genes in Apex EECs

A consequence of low shear stress is increased residence time of blood components that can contribute to hemostasis with increased risk for thrombus formation. Based on calculations of OSI in the apex and measurements of blood residence time by others,[10] the apex represents a potentially prothrombotic environment. Healthy persons, however, do not typically form thrombi in the apex, an outcome that may be attributable in part to regional expression of anticoagulation genes.

Tissue factor pathway inhibitor (TFPI) is produced by ECs and is the principal inhibitor of tissue factor,[23] the key initiator of the coagulation cascade. TFPI was identified by RNAseq as upregulated 20-fold in the LV apex compared with the base. Validation by qPCR showed a mean increase of 50-fold (range 15- to 100-fold) in apex EECs relative to base EECs (Figure 8A); therefore, TFPI may play a role as a potent anticoagulant in preventing clot formation in the LV apex. Furthermore, RNAseq identified differential expression of prostacyclin synthase (PTGIS) in the apex. Prostacyclin

Table 3. Top Canonical Pathways Predicted by Ingenuity Pathway Analysis for the 833 Differentially Expressed Genes Specific to Base:Apex Comparison

Canonical Pathway	*P* Value	Molecules Represented
eIF2 signaling	$4.5\times^{10}-24$	45/185
mTOR signaling	$1.1\times^{10}-10$	29/188
Regulation of eIF4 and p70S6K Signaling	$1.4\times^{10}-07$	21/146
Mitochondrial dysfunction	$2.0\times^{10}-06$	21/171
Oxidative phosphorylation	$6.1\times^{10}-05$	14/109

eIF indicates eukaryotic initiation factor; mTOR, mammalian target of rapamycin.

synthase, the primary enzyme responsible for production of prostacyclin, an integral inhibitor of platelet activation,[24] was 5-fold higher in the LV apex than base EECs (Figure 8B).

In addition to soluble and membrane-bound factors produced by ECs, the endothelial glycocalyx represents an important barrier to the activation of coagulation.[25] This surface layer provides electrical repulsion of activated platelets via its strong negative charge. The endothelial glycocalyx enzyme heparan sulfate 6-O-sulfotransferase 2 (HS6ST2), which catalyzes the transfer of sulfate to heparan sulfate, was identified as a DEG and was validated by qPCR as upregulated 5-fold in the apex (range 2- to 10-fold) (Figure 8C). Furthermore, the endothelial membrane receptor neuropilin 1, a glycocalyx proteoglycan,[26] was also upregulated by 5-fold (range 2- to 12-fold) (Figure 8D) in the LV apex versus the base.

Discussion

The endothelium is a heterogeneous dynamic interface able to functionally adapt to a wide variety of chemical, biophysical, and biomechanical stimuli. In this study, we reported spatial WSS in defined regions of human and pig LV, identified temporal WSS in each region during the cardiac cycle, and demonstrated important regional differences in endocardial gene expression.

Significant differences in WSS magnitude and axial WSS between the LV base and the LV apex were common to both species studied. The low flow regions of the LV generally do not express a proinflammatory EEC phenotype; however, thrombi are commonly located in the apex in heart failure patients.[27]

A well-established concept in arterial endothelial biology is the cause–effect relationship between hemodynamic WSS and gene expression.[1,28–30] In this study, we identified the regional patterning of WSS and EEC phenotype but have not yet isolated the mechanisms to explain their relationships and how they may be different or similar to arterial ECs. Speculative mechanisms attributable to regionally different LV EEC gene expression may include (1) additional biomechanical effects of complex hemodynamics on EEC phenotype; (2) developmental (in contrast to environmental) programming of EEC phenotypes related to each LV region; (3) molecular transport characteristics, particularly those related to prolonged blood retention in the LV apex; and/or (4) a combination of flow, developmental, and transport mechanisms.

Additional Biomechanical Effects of Complex Hemodynamics

In addition to shear stress, blood imparts volumetric changes that exert circumferential stretch (or strain) on the vessel wall. The effects of WSS and circumferential stretch on ECs are typically studied in isolation. Qiu and Tarbell,[31] however, have demonstrated that the temporal relationship between the WSS and circumferential stretch can have unique effects on EC biology independent of either stress alone. Shifts in this spatiotemporal relationship, termed *stress phase angle*, have been shown to influence production of paracrine factors (ie, nitric oxide, prostacyclin) and endothelial gene expression.[32] Although we were unable to measure aspects of circumferential stretch from our imaging data, it is possible that the concerted spatial and temporal nature of the hemodynamic forces on the endocardium affect regional heterogeneity of gene expression.

Previous studies have demonstrated that loss of TFPI promotes vascular thrombosis,[33] thus the elevated expression of TFPI and PTGIS in the apex may inhibit thrombosis at a location at which OSI is elevated, WSS is low, and blood residence time is significantly increased. These data contrast with reports of arterial EC experiments in vitro that showed no effect of oscillatory flow on TFPI gene expression.[34–36] Nevertheless, a step increase of WSS resulted in a marked increase in TFPI expression[35] suggesting that rate of change of WSS and the associated circumferential stretch may be important for TFPI transcriptional regulation. Mouse models of pressure overload also support a role for strain regulation of TFPI in vivo, in which filling pressure of the left atrium contributed to increased TFPI expression.[37]

Developmental Programming

Flow is essential for successful heart and valve formation, in which endothelial phenotype programming plays a central role.[4,38] Flow may continue to define the EEC phenotype in the fully mature heart against a “fixed” developmental background. A broad distinction between flow and developmental mechanisms may be tested by analyzing EEC phenotype after experimentally modifying regional flow

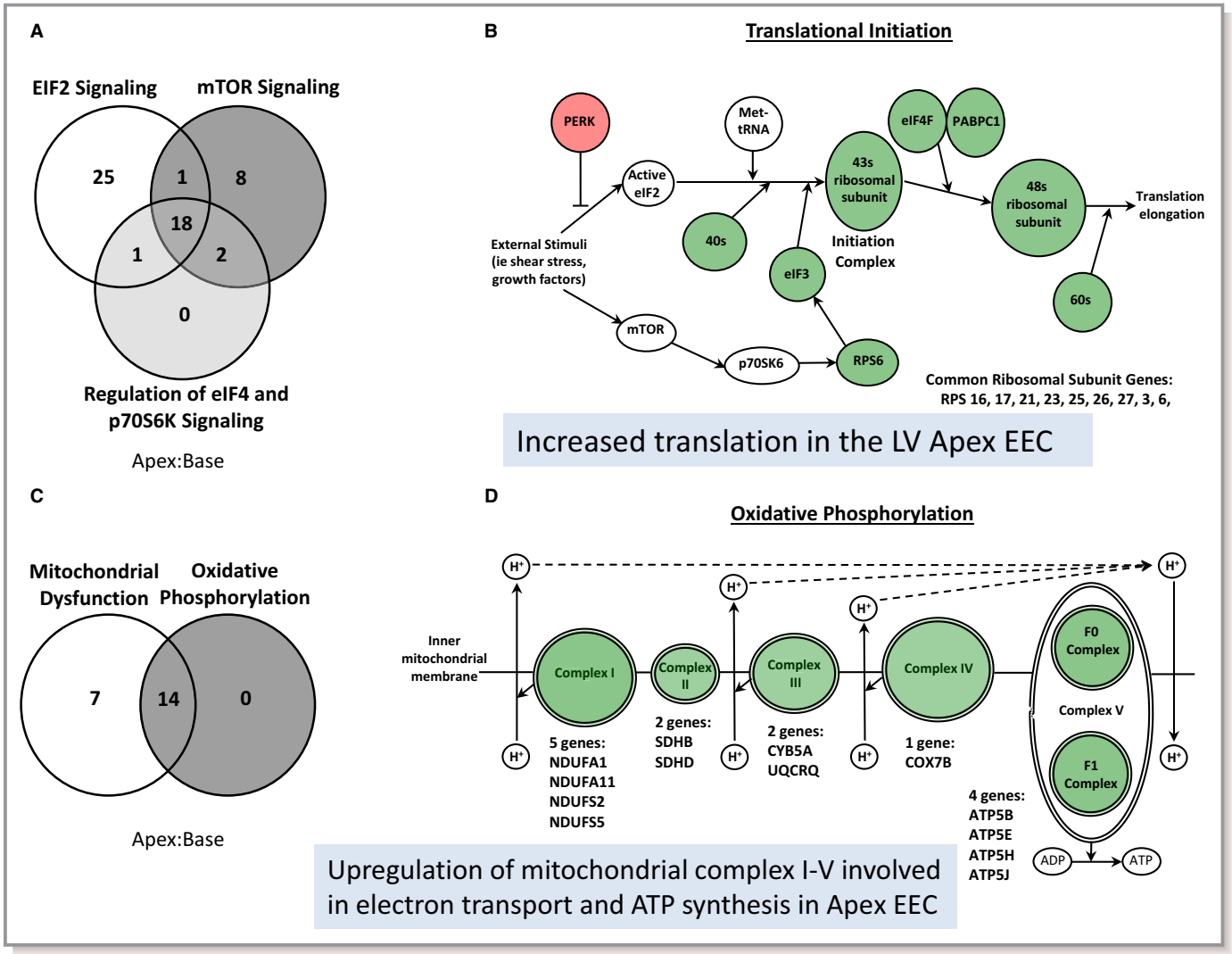

Figure 7. Analysis of signaling pathways specific to base:apex comparison. A, Venn diagram comparing overlap of genes identified in the top 3 canonical pathways: eIF2 signaling, mTOR signaling, and regulation of eIF4 and p70S6K signaling. In total, 18 genes were identified in common. B, Schematic of translation initiation with genes/complexes associated with the DEG list identified. Shaded in green are genes that are upregulated in the apex. C, Venn diagram of genes of mitochondrial dysfunction and oxidative phosphorylation. No genes were unique to oxidative phosphorylation. D, Schematic of oxidative phosphorylation. Genes identified in each complex are listed. For (B and D), red indicates genes/complexes that are downregulated, green indicates genes/complexes that are upregulated in the LV apex, and white indicates genes/complexes that are not represented on the DEG list but are important to pathway. DEG indicates differentially expressed gene; EEC, endocardial endothelial cell; eIF, eukaryotic initiation factor; LV, left ventricle; mTOR, mammalian target of rapamycin.

characteristics in the mature heart (eg, by mitral annuloplasty)[39] to establish the extent of hemodynamic cause and effect.

Molecular Transport Kinetics at the Cell Surface

Although hemodynamic forces (WSS, CS) are the main mechanical deformations influencing endothelial mechanotransduction, similar cell signaling responses are also inducible by changes in molecular transport of labile biochemicals in the bulk fluid at the endothelial surface.[40] The relative contribution of this indirect mechanism to flow-mediated endothelial signaling and whether it could influence steady-state cell phenotype in the apex is unknown. The retention of blood in the apex for a longer period[10] likely leads to quite different average transport kinetics at the apical EEC surface that may influence cell phenotype.

The possibility that contraction/relaxation of the underlying muscle also contributes to the EEC phenotype cannot be excluded.[41] Studies using computed tomography imaging in normal adult pigs suggest that regional differences in stretching of the endocardium are minimal or undetectable[42]; however, the resolution of the imaging in these studies (200–300 μm) is 2 to 3 orders of magnitude too low to detect cell

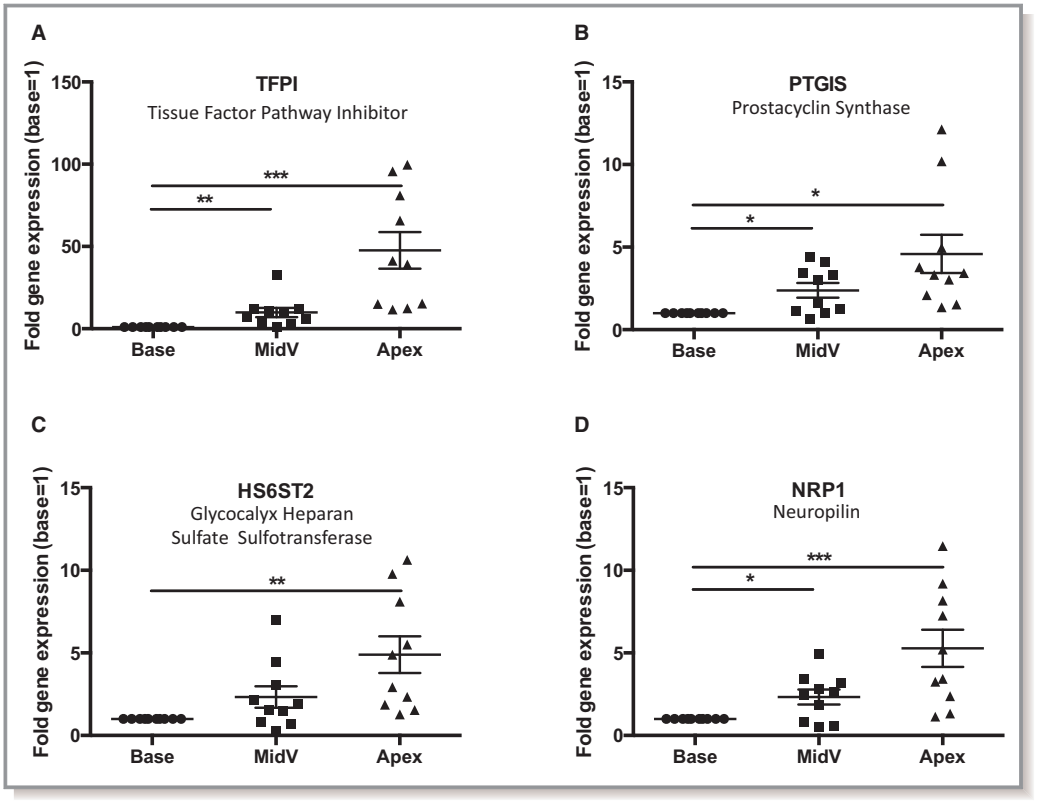

Figure 8. Upregulation of anticoagulant genes in left ventricle apex. The mRNA expression by quantitative polymerase chain reaction for genes in the base, midV, and apex. Fold change of gene expression relative to base=1. A, TFPI, (B) PTGIS, (C) HS6ST2, and (D) NRP1. For each gene assayed, n=10. Data represent mean±SEM. **P*<0.05, ***P*<0.01, ****P*<0.005. HS6ST2 indicates heparan sulfate 6-O-sulfotransferase 2; midV, midventricle; NRP1, neuropilin 1; PTGIS, prostaglandin I_2 (prostacyclin) synthase; TFPI, tissue factor pathway inhibitor.

deformation. In vitro studies of phenotype shift in EECs subjected to controlled stretch may clarify the mechanism.

Although both MRI analysis and RNAseq identified differences among base, midV, and apex, the greatest differences were found between base and apex; therefore, we prioritized RNAseq analysis of this comparison. We categorized the top 5 predicted canonical pathways into 2 connected biological functions: translation initiation and oxidative phosphorylation. Both translation and oxidative phosphorylation represent fundamental cellular pathways, and the influence of each can have significant effects on metabolic homeostasis. It is possible that a consequence of the involvement of these pathways is an endothelial environment more primed for response to alternating stimuli.

Moreover, mTOR, a protein kinase primarily associated with regulating translation, is also known to influence cell proliferation via regulation of downstream effectors[43]: Inhibition of mTOR blocks proliferation as well as cell growth. Our sequencing data suggest that the mTOR pathway is upregulated in the apex, possibly implicating elevated proliferation in this region. This fits with previous observations that oscillatory shear stress enhances EC turnover via SMAD1/5-mediated mTOR activation.[44] In addition, mTOR signaling has been shown to mediate mitochondrial oxidative function via regulation of mitochondrial genes,[45] which may explain why oxidative phosphorylation rose to prominence in the DEG analyses.

The identification of oxidative phosphorylation is an interesting observation, given that arterial ECs rely primarily on glycolysis for their energy production. In vitro estimates suggest that 75% to 90% of EC energy is derived from glycolysis and very little from oxidative phosphorylation.[46] Because of their limited number and the reliance on glycolysis, endothelial mitochondria are understudied and generally regarded for their reactive oxygen species–producing capabilities. The potential for increased oxidative phosphorylation may also represent a shift in substrate use toward fatty acid oxidation. To this end, IPA predicted increased accumulation of fatty acid in the apex based on the gene expression profile.

Regional differences in gene expression may have functional consequences for the underlying myocardium. Studies over the past 3 decades have elucidated an important role for endocardium in cardiomyocyte contraction.[2] This is due in

part to the production and release of molecules such as nitric oxide, endothelin, and neuregulin 1.[47] Based on the integral role that shear stress plays in endothelial gene expression and function, it is possible that communication between EECs and cardiomyocytes varies by region within the LV. Furthermore, perturbation of LV hemodynamics (eg, following mitral annuloplasty, myocardial infarction) may result not only in altered EEC function but also altered cardiomyocyte and myocardial function. In this context, EECs may represent a selective target in addressing cardiomyopathies.

Acknowledgments

We thank Dr Juan M. Jiménez for critical comments.

Sources of Funding

Supported by NIH NRSA Training Grant T32 HL07954 (McCormick), NIH P01 HL06220 (Davies), AHA Postdoctoral Fellowship 13POST14070010 (Jiang), NIH R00 HL108157 (Witschey), NIH R01 HL073021 (Gorman), NIH R01 HL115828 (Markl), and NIH K25 HL119608 (Barker).

Disclosures

None.

References

1. Davies PF, Civelek M, Fang Y, Fleming I. The atherosusceptible endothelium: endothelial phenotypes in complex haemodynamic shear stress regions in vivo. *Cardiovasc Res*. 2013;99:315–327.
2. Mebazaa A, Mayoux E, Maeda K, Martin LD, Lakatta EG, Robotham JL, Shah AM. Paracrine effects of endocardial endothelial cells on myocyte contraction mediated via endothelin. *Am J Physiol Heart Circ Physiol*. 1993;34:H1841–H1846.
3. Mebazaa A, Wetzel R, Cherian M, Abraham M. Comparison between endocardial and great vessel endothelial cells: morphology, growth and prostaglandin release. *Am J Physiol Heart Circ Physiol*. 1995;268:H250–H259.
4. Hove JR, Köster RW, Forouhar AS, Acevedo-Bolton G, Fraser SE, Gharib M. Intracardiac fluid forces are an essential epigenetic factor for embryonic cardiogenesis. *Nature*. 2003;421:172–177.
5. Icardo JM. Endocardial cell arrangement: role of hemodynamics. *Anat Rec*. 1989;225:150–155.
6. Hanada T, Hashimoto M, Nosaka S, Sasako T, Nakayama K, Masumura S, Yamauchi M, Tamura K. Shear stress enhances prostacyclin release from endocardial endothelial cells. *Life Sci*. 2000;66:215–220.
7. Rodriguez Muñoz D, Markl M, Moya Mur JL, Barker A, Fernández-Golfín C, Lancellotti P, Zamorano Gómez JL. Intracardiac flow visualization: current status and future directions. *Eur Heart J Cardiovasc Imaging*. 2013;14:1029–1038.
8. Gharib M, Rambod E, Kheradvar A, Sahn DJ, Dabiri JO. Optimal vortex formation as an index of cardiac health. *Proc Natl Acad Sci USA*. 2006;103:6305–6308.
9. Markl M, Frydrychowicz A, Kozerke S, Hope M, Wieben O. 4D flow MRI. *J Magn Reson Imaging*. 2012;36:1015–1036.
10. Hendabadi S, Bermejo J, Benito Y, Yotti R, Fernández-Avilés F, Del Álamo JC, Shadden SC. Topology of blood transport in the human left ventricle by novel processing of Doppler echocardiography. *Ann Biomed Eng*. 2013;41:2603–2616.
11. Föll D, Taeger S, Bode C, Jung B, Markl M. Age, gender, blood pressure, and ventricular geometry influence normal 3D blood flow characteristics in the left heart. *Eur Heart J Cardiovasc Imaging*. 2013;14:366–373.
12. Markl M, Harloff A, Bley TA, Zaitsev M, Jung B, Weigang E, Langer M, Hennig J, Frydrychowicz A. Time-resolved 3D MR velocity mapping at 3T: improved navigator-gated assessment of vascular anatomy and blood flow. *J Magn Reson Imaging*. 2007;25:824–831.
13. Stalder AF, Russe MF, Frydrychowicz A, Bock J, Hennig J, Markl M. Quantitative 2D and 3D phase contrast MRI: optimized analysis of blood flow and vessel wall parameters. *Magn Reson Med*. 2008;60:1218–1231.
14. Jiang YZ, Manduchi E, Stoeckert CJ Jr, Davies PF. Arterial endothelial methylome: differential DNA methylation in athero-susceptible disturbed flow regions in vivo. *BMC Genomics*. 2015;16:506.
15. Dobin A, Davis CA, Schlesinger F, Drenkow J, Zaleski C, Jha S, Batut P, Chaisson M, Gingeras TR. STAR: ultrafast universal RNA-seq aligner. *Bioinformatics*. 2013;29:15–21.
16. Robinson MD, McCarthy DJ, Smyth GK. edgeR: a Bioconductor package for differential expression analysis of digital gene expression data. *Bioinformatics*. 2010;26:139–140.
17. Grant GR, Liu J, Stoeckert CJ Jr. A practical false discovery rate approach to identifying patterns of differential expression in microarray data. *Bioinformatics*. 2005;21:2684–2690.
18. Huang da W, Sherman BT, Lempicki RA. Bioinformatics enrichment tools: paths toward the comprehensive functional analysis of large gene lists. *Nucleic Acids Res*. 2009;37:1–13.
19. Huang da W, Sherman BT, Lempicki RA. Systematic and integrative analysis of large gene lists using DAVID bioinformatics resources. *Nat Protoc*. 2009;4:44–57.
20. Davies PF. Flow-mediated endothelial mechanotransduction. *Physiol Rev*. 1995;75:519–560.
21. Isoda H, Ohkura Y, Kosugi T, Hirano M, Takeda H, Hiramatsu H, Yamashita S, Takehara Y, Alley MT, Bammer R, Pelc NJ, Namba H, Sakahara H. In vivo hemodynamic analysis of intracranial aneurysms obtained by magnetic resonance fluid dynamics (MRFD) based on time-resolved three-dimensional phase-contrast MRI. *Neuroradiology*. 2010;52:921–928.
22. Kraiss LW, Weyrich AS, Alto NM, Dixon DA, Ennis TM, Modur V, McIntyre TM, Prescott SM, Zimmerman GA. Fluid flow activates a regulator of translation, p70/p85 S6 kinase in human endothelial cells. *Am J Physiol Heart Circ Physiol*. 2000;278:H1537–H1544.
23. Wood JP, Ellery PE, Maroney SA, Mast AE. Biology of tissue factor pathway inhibitor. *Blood*. 2014;123:2934–2943.
24. Moncada S, Gryglewskit R, Bunting S, Vane JR. An enzyme isolated from arteries transforms prostaglandin endoperoxides to an unstable substance that inhibits platelet aggregation. *Nature*. 1976;263:663–665.
25. Reitsma S, Slaaf DW, Vink H, van Zandvoort MA, oude Egbrink MG. The endothelial glycocalyx: composition, functions, and visualization. *Pflugers Arch*. 2007;454:345–359.
26. Shintani Y, Takashima S, Asano Y, Kato H, Liao Y, Yamazaki S, Tsukamoto O, Seguchi O, Yamamoto H, Fukushima T, Sugahara K, Kitakaze M, Hori M. Glycosaminoglycan modification of neuropilin-1 modulates VEGFR2 signaling. *EMBO J*. 2006;25:3045–3055.
27. Bettari L, Fiuzat M, Becker R, Felker GM, Metra M, O'Connor CM. Thromboembolism and antithrombotic therapy in patients with heart failure in sinus rhythm: current status and future directions. *Circ Heart Fail*. 2011;4:361–368.
28. Davies PF. Hemodynamic shear stress and the endothelium in cardiovascular pathophysiology. *Nat Clin Pract Cardiovasc Med*. 2009;6:16–26.
29. Civelek M, Manduchi E, Riley RJ, Stoeckert CJ Jr, Davies PF. Chronic endoplasmic reticulum stress activates unfolded protein response in arterial endothelium in regions of susceptibility to atherosclerosis. *Circ Res*. 2009;105:453–461.
30. Won D, Zhu SN, Chen M, Teichert AM, Fish JE, Matouk CC, Bonert M, Ojha M, Marsden PA, Cybulsky MI. Relative reduction of endothelial nitric-oxide synthase expression and transcription in atherosclerosis-prone regions of the mouse aorta and in an in vitro model of disturbed flow. *Am J Pathol*. 2007;171:1691–1704.
31. Qiu Y, Tarbell JM. Interaction between wall shear stress and circumferential strain affects endothelial cell biochemical production. *J Vasc Res*. 2000;37:147–157.
32. Amaya R, Pierides A, Tarbell JM. The interaction between fluid wall shear stress and solid circumferential strain affects endothelial gene expression. *PLoS One*. 2015;10:e0129952.
33. Westrick RJ, Bodary PF, Xu Z, Shen Y-C, Broze GJ, Eitzman DT. Deficiency of tissue factor pathway inhibitor promotes atherosclerosis and thrombosis in mice. *Circulation*. 2001;103:3044–3046.

34. Mazzolai L, Silacci P, Bouzourene K, Daniel F, Brunner H, Hayoz D. Tissue factor activity is upregulated in human endothelial cells exposed to oscillatory shear stress. *Thromb Haemost*. 2002;87:1062–1068.
35. Grabowski EF, Reininger AJ, Petteruti PG, Tsukurov O, Orkin RW. Shear stress decreases endothelial cell tissue factor activity by augmenting secretion of tissue factor pathway inhibitor. *Arterioscler Thromb Vasc Biol*. 2001;21:157–162.
36. Westmuckett AD, Lupu C, Roquefeuil S, Krausz T, Kakkar VV, Lupu F. Fluid flow induces upregulation of synthesis and release of tissue factor pathway inhibitor in vitro. *Arterioscler Thromb Vasc Biol*. 2000;20:2474–2482.
37. Kapur NK, Deming CB, Kapur S, Bian C, Champion HC, Donahue JK, Kass DA, Rade JJ. Hemodynamic modulation of endocardial thromboresistance. *Circulation*. 2007;115:67–75.
38. Dietrich AC, Lombardo VA, Veerkamp J, Priller F, Abdelilah-Seyfried S. Blood flow and BMP signaling control endocardial chamber morphogenesis. *Dev Cell*. 2014;30:367–377.
39. Witschey WR, Zhang D, Contijoch F, McGarvey JR, Lee M, Takebayashi S, Aoki C, Han Y, Han J, Barker AJ, Pilla JJ, Gorman RC, Gorman JH III. The influence of mitral annuloplasty on left ventricular flow dynamics. *Ann Thorac Surg*. 2015;100:114–121.
40. Dull RO, Tarbell JM, Davies PF. Mechanisms of flow-mediated signal transduction in endothelial cells: kinetics of ATP surface concentrations. *J Vasc Res*. 1992;29:410–419.
41. Vis MA, Bovendeerd PHM, Sipkema P, Westerhof N. Effect of ventricular contraction, pressure, and wall stretch on vessels at different locations in the wall. *Am J Physiol Heart Circ Physiol*. 1997;272:H2963–H2975.
42. Pourmorteza A, Schuleri KH, Herzka DA, Lardo AC, McVeigh ER. A new method for cardiac computed tomography regional function assessment: stretch quantifier for endocardial engraved zones (SQUEEZ). *Circ Cardiovasc Imaging*. 2012;5:243–250.
43. Fingar DC, Richardson CJ, Tee AR, Cheatham L, Tsou C, Blenis J. mTOR controls cell cycle progression through its cell growth effectors S6K1 and 4E-BP1/eukaryotic translation initiation factor 4E. *Mol Cell Biol*. 2003;24:200–216.
44. Zhou J, Lee P, Tsai C, Lee C, Yang T, Chuang H, Lin W, Lin T, Lim SH, Wei S, Chen Y, Chien S, Chiu JJ. Force-specific activation of Smad1/5 regulates vascular endothelial cell cycle progression in response to disturbed flow. *Proc Natl Acad Sci USA*. 2012;109:7770–7775.
45. Cunningham JT, Rodgers JT, Arlow DH, Vazquez F, Mootha VK, Puigserver P. mTOR controls mitochondrial oxidative function through a YY1-PGC-1alpha transcriptional complex. *Nature*. 2007;450:736–740.
46. Eelen G, de Zeeuw P, Simons M, Carmeliet P. Endothelial cell metabolism in normal and diseased vasculature. *Circ Res*. 2015;116:1231–1244.
47. Brutsaert DL. Cardiac endothelial-myocardial signaling: its role in cardiac growth, contractile performance, and rhythmicity. *Physiol Rev*. 2003;83:59–115.

SUPPLEMENTAL MATERIALS

Supplemental Materials and Methods

Protein isolation and Western blots

Freshly isolated endocardial endothelial cells were placed directly into 100 µl ice-cold RIPA buffer containing 25 mmol/L Tris-Cl pH 7.6, 1 mmol/L EDTA, 150 mmol/L NaCl, 1% Triton X-100, 0.5% Sodium deoxycholate, 0.1% sodium dodecyl sulfate plus protease and phosphatase inhibitor cocktails (EMD Millipore, Billerica, MA). Samples were sonicated on ice using three 10 second pulses then centrifuged at 10,000 rpm for 60 minutes at 4°C. The supernatant was collected and placed in a new micro-centrifuge tube. The Pierce BCA Assay was used to measure protein concentrations (ThermoFisher Scientific, Waltham, MA). Samples were then mixed with 10X LSB to a final concentration of 2X.

Approximately 25 µg of total protein per sample were run on 4-12% Bis-Tris precast gels (Invitrogen, ThermoFisher, Waltham,MA) then transferred to PVDF membranes for Western blot analysis using antibodies to CD31/PECAM-1 (M-20) (Santa Cruz Biotechnology, Inc. Santa Cruz, CA), Vimentin and Vinculin (Chemicon, EMD Millipore, Billerica, MA), and Cardiac Troponin I (Abcam, Cambridge, MA).

Immunofluorescence

Endothelial cells isolated from base, midV and apex were fixed onto microscope slides using 2% formaldehyde. The cells were rinsed, then permeabilized using 0.2% Triton X-100 in phosphate buffered saline. Following permeabilization, the slides were blocked using 10% goat serum for 60 minutes at room temperature, incubated with

primary antibody solutions overnight at 4°C, then rinsed and incubated with secondary antibody for 60 minutes at room temperature. Following washing, the slides were mounted using Vectashield plus DAPI (Vector Labs, Burlingame, CA).

Supplemental Tables

Table S1. Human Volunteer Characteristics

	Mean ± SD (n = 8, 4 males and 4 females)	**Range**
Age	24.1 ± 1.8	[21.2, 26.1]
Heart Rate (BPM)	63.5 ± 8.7	[52, 76]
LVEF (%)	65.3 ± 2.1	[57, 69]

BPM, beats per minute; LVEF, left ventricular ejection fraction

Table S2. Mean absolute error between observers

	Human			Pig		
	Base	**MidV**	**Apex**	**Base**	**MidV**	**Apex**
Wall Shear Stress (Pa)						
Magnitude	0.02 (0.14)	0.10 (0.07)	0.03 (0.03)	0.02 (0.04)	0.12 (0.07)	0.04 (0.03)
Axial						
Peak Inflow	0.15 (0.17)	0.11 (0.08)	0.03 (0.04)	0.33 (0.13)	0.13 (0.07)	0.02 (0.03)
Peak Outflow	0.11 (0.15)	0.06 (0.05)	0.03 (0.03)	0.002 (0.05)	0.05 (0.04)	0.007 (0.01)
Circumferential						
Max	0.04 (0.08)	0.004 (0.005)	2.4E-5 (0.007)	0.37 (0.33)	0.02 (0.03)	0.0004 (0.006)
Min	0.001 (0.02)	0.001 (0.009)	0.007 (0.009)	0.009 (0.02)	0.02 (0.02)	0.01 (0.02)
Oscillatory Shear Index						
3D	5.45 (5.16)	1.36 (2.16)	0.07 (1.57)	1.21 (2.70)	0.35 (3.42)	0.80 (1.87)
Axial	7.11 (6.38)	4.08 (5.06)	0.90 (0.97)	1.65 (3.29)	1.61 (4.94)	3.31 (2.24)
Circumferential	2.41 (2.64)	0.19 (1.21)	1.17 (2.22)	3.17 (4.65)	4.79 (6.18)	1.83 (3.37)

The standard deviation of the error between samples is given in parenthesis

Table S3. Primer sequences for porcine genes

Gene	Forward 5' → 3'	Reverse 5' → 3'
ABCA1	CCC CTG TGG TCT TTC TGG ATG A	ACT TAG GGC ACA ATT CCA CAA GA
ACAA2	GGC AAC GTC TCT CCT GAA AC	AAC CAG AGC CAC AGA GCC TA
APOA1	CGA TCA AAG ACA GTG GCA GA	GCT GCA CCT TCT TCT TCA CC
CCND1	GCC TCG AAG ATG AAG GAG AC	TTG GAG AGG AAG TGC TCG AT
CIDEC	TGG CAG ACA AGC CTT TCT TT	AGT CCT GTG GGT TCA CCT TG
CLDN5	CTG GAC CAC AAC ATC GTG AC	CTG CCA AGG TAA CGA AGA GC
EIF2AK3	CCA GCC TTA GCA AAC C	ACT ATA TGC ACT GAG TCC G
EIF3H	GGA AGA ACC TCC AGT TGC TG	ACT CTG GCG CTG CAT ATT CT
EIF4B	GAT TCC AGG ATA GGC AGT GG	CCT CTA TCA TCA CGC CGA TAA
FABP3	TCA AGC TGG GAG TGG AGT TT	CAT GGG TGA GTG TCA GGA TG
GAPDH	CCT GTG ACT TCA ACA GTG ACA C	CCC TGT TGC TGT AGC CAA ATT C
HSPA5	CCT ACT CGT GCG TTG G	CTG CAC AGA CGG GTC A
HS6ST2	CTC CTG CGC AAG GTA GAC TT	TGG CAA GTG CAT TTC TTC TG
VEGFR2	TCA CAA TTC CAA AAG TGA TCG G	GGT CAC TAA CAG AAG CAA TAA ATG G
NRP1	AGG CTT CTC GGC AAA CTA CA	AGG CCC AAG TCT ACC TGG AT
PABPC1	ATG GCA GCT ATC CCA CAG AC	GGA CAT GAC TCG TGG AAC CT
RPS10	TTT CAA GGA GGG AGT GAT GG	GGT GGA GGT AAT CAC GGA GA
PTGIS	TCC TGG ACC CAC ACT CCT AC	GAC AGT GCG GAG GTT GGT AT
TFPI	GCT GCC TTG GCA ATC TAA AC	GAA GCT GGG TGC TTT GGT AG
TP53	CGA ACT GGC TGG ATG AAA AT	ACT TGG CTG TTC CAG AAT GC

Table S4. Top canonical pathways as predicted by IPA analysis (FDR 0.10)

	Canonical Pathway	p-value	Molecules Represented
Base:Apex			
	eIF2 Signaling	8.3E-28	59
	mTOR signaling	4.8E-14	39
	Regulation of eIF4 and p70S6K signaling	1.1E-10	30
	Fatty Acid β-oxidation	5.3E-06	10
	LPS/IL-1 Mediated Inhibition of RXR Function	9.4E-06	27
Base:MidV			
	eIF2 Signaling	3.6E-08	15
	Regulation of eIF4 and p70S6K Signaling	1.7E-04	9
	mTOR Signaling	2.5E-04	10
	Agranulocyte Adhesion and Diapedesis	2.6E-04	10
	Hepatic Fibrosis/Stellate Cell Activation	3.7E-04	10

Table S5. Overrepresented biological functions identified by DAVID

Functional Category	No. of Genes DE*	P+	Functional Category	No. of Genes DE#	P+
Base:Apex			**Base:MidV**		
Translational elongation	46	1.2E-30	Muscle contraction	18	8.5E-10
Translation	66	2.1E-20	Muscle system process	18	3.6E-09
Oxidation Reduction	71	8.1E-09	Translational elongation	13	1.3E-07
Regulation of cell growth	28	5.1E-06	Striated muscle contraction	9	8.9E-07
Regulation of developmental growth	12	2.9E-05	Actin filament-based movement	7	1.7E-06
Regulation of axon extension	8	5.3E-05	Cardiac muscle tissue development	9	4.8E-06
Blood vessel development	30	5.3E-05	Cardiac muscle tissue morphogenesis	7	4.8E-06
Regulation of cell morphogenesis	20	7.1E-05	Muscle tissue morphogenesis	7	4.8E-06
Vasculature development	30	8.2E-05	Regulation of ATPase activity	6	5.0E-06
Regulation of growth	37	8.2E-05	Actomyosin structure organization	7	6.1E-06

*Base:apex compared, #Base:midV compared,

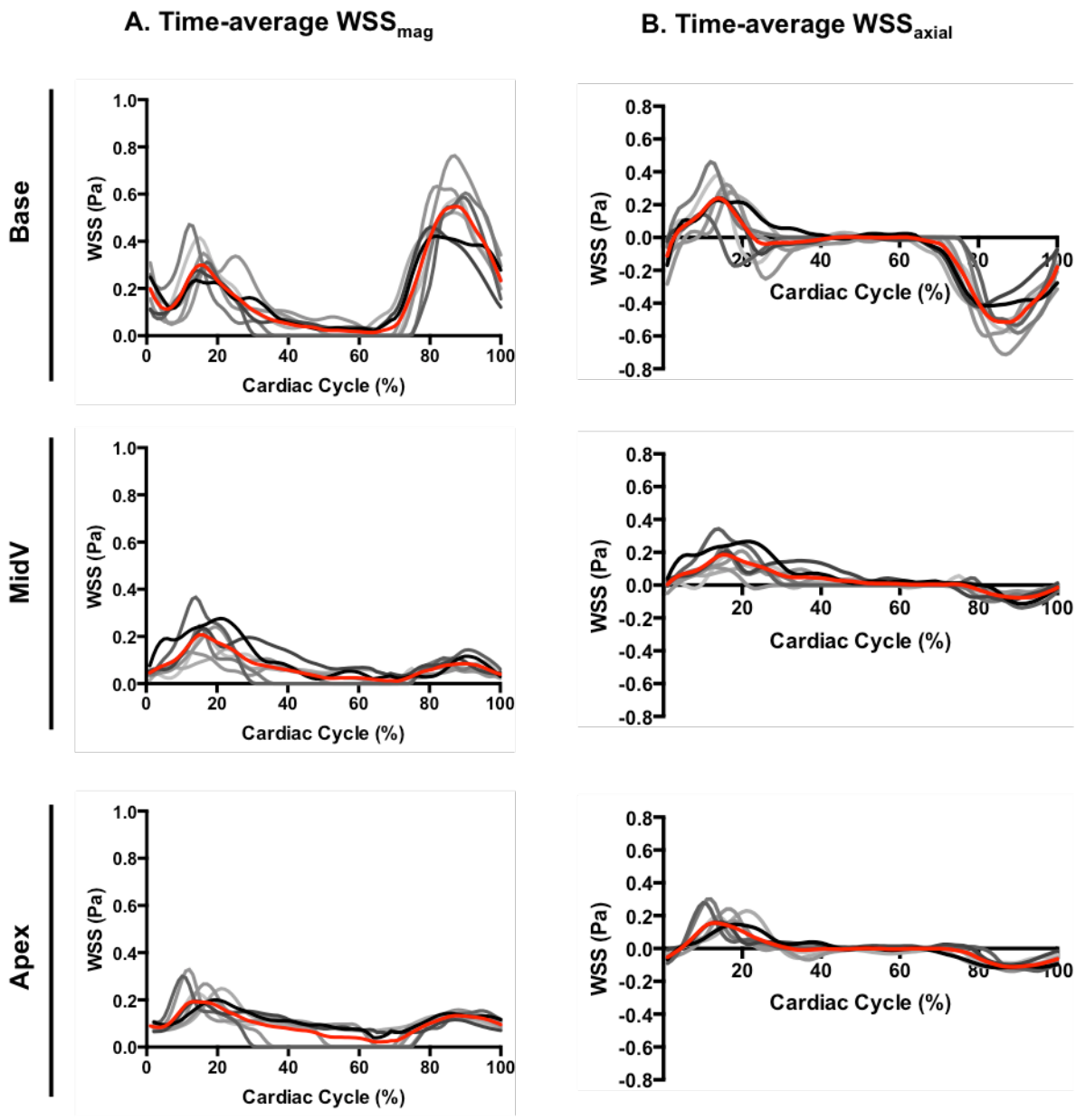

Figure S1. 4D Flow MRI Analysis of HUMAN endocardial WSS A, Time-averaged WSS_{mag} and B, Time-averaged WSS_{axial} values are shown for individual volunteers (n=8) (gray lines) and the average (red line) for the three regions of interest.

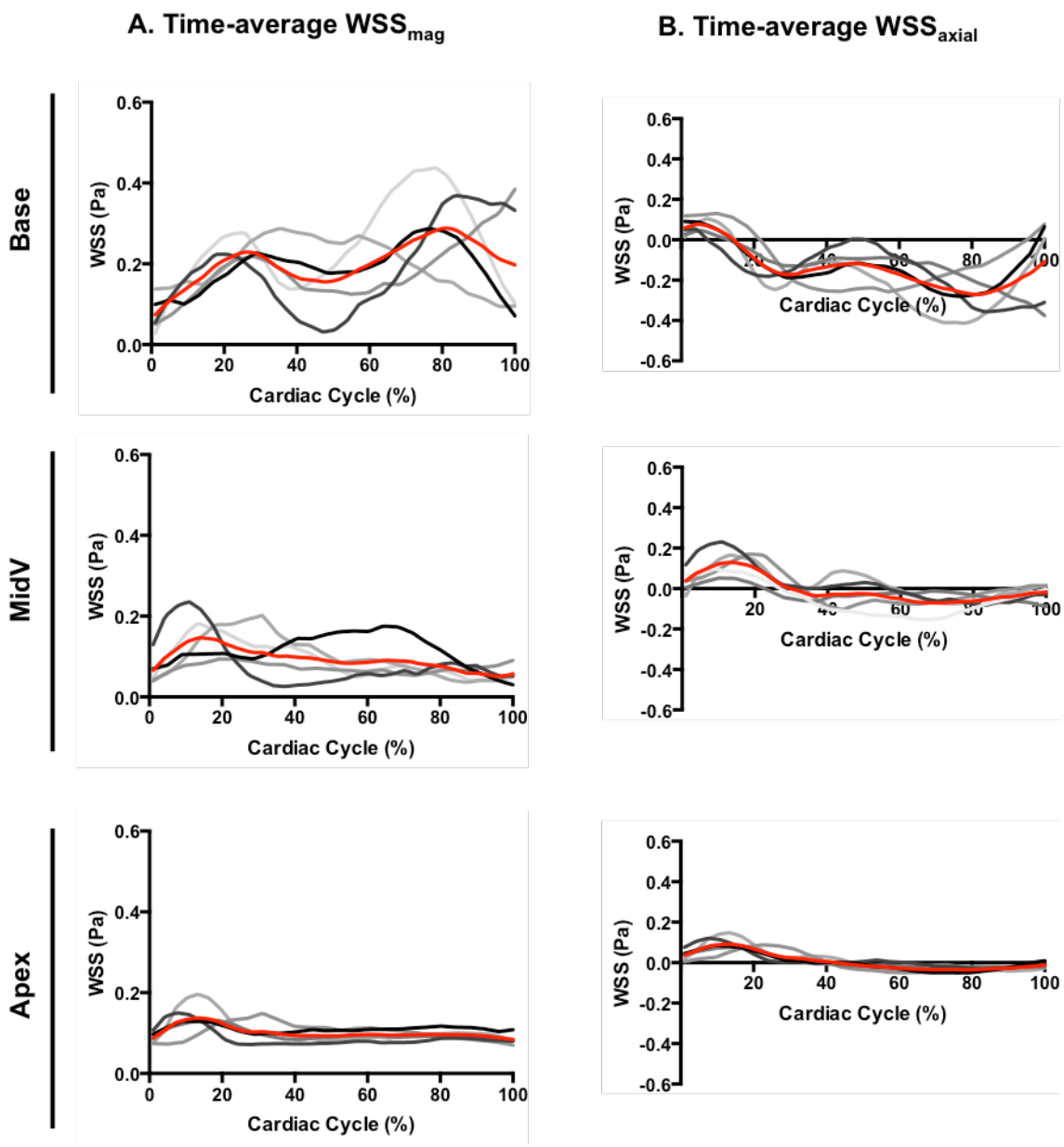

Figure S2. 4D Flow MRI Analysis of PIG endocardial WSS A, Time-averaged WSS_{mag} and B, Time-averaged WSS_{axial} values are shown for individual pigs (n=5) (gray lines) and the average (red line) for the three regions of interest.

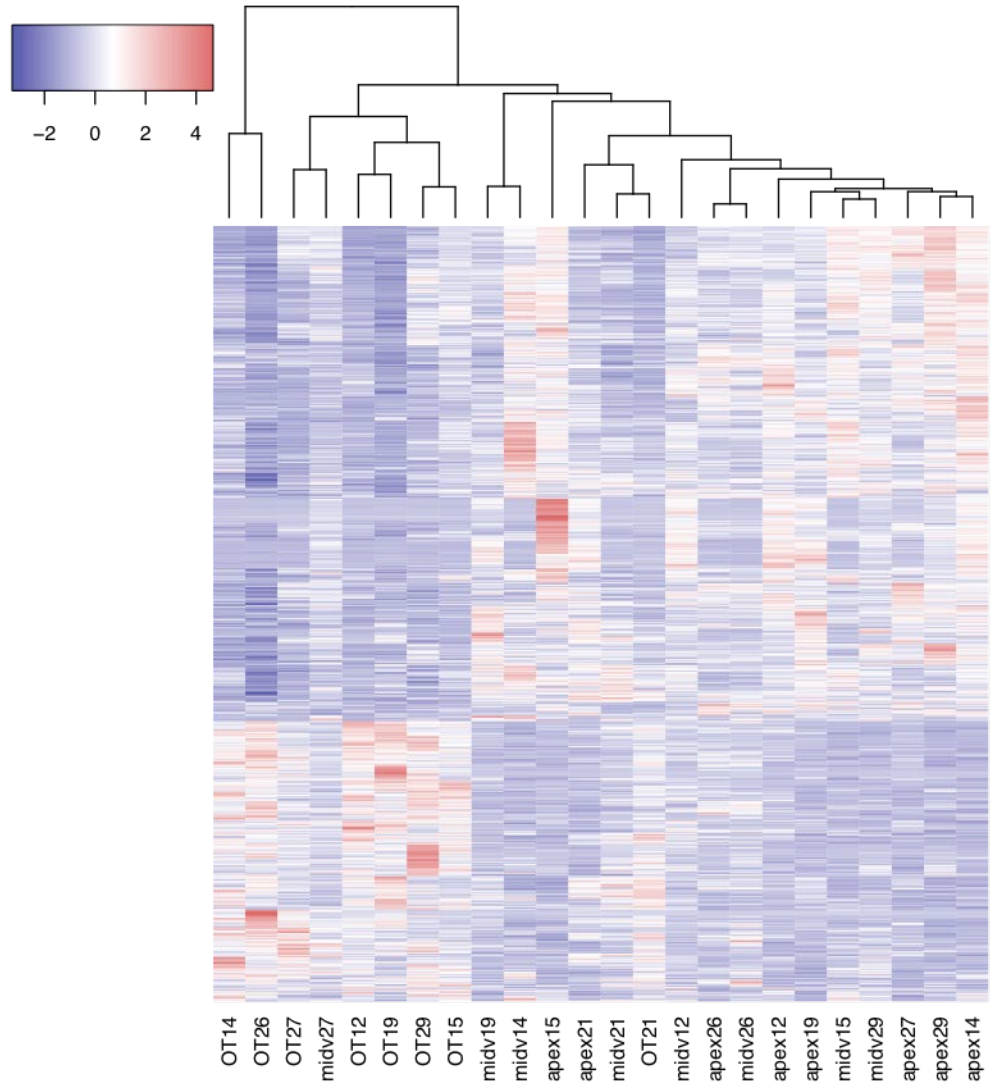

Figure S3. Hierarchical clustering of DEGs between regions. Hierarchical clustering of the rows and columns (method = average, similarity measure = Pearson correlation). OT refers to base samples, numbers following region indicate individual sample number.

Supplemental Movie Legend

Movie S1: Visualization of blood flow in the left ventricle (LV) of a pig during a complete cardiac cycle calculated from 4D flow MRI by the methods of Markl et al[1]. Prospective ECG-gated time-resolved phase contrast MRI with three directional velocity encoding was employed to measure blood flow velocity with full volumetric coverage of the LV.

Reference:

1. Markl M, Harloff A, Bley TA, Zaitsev M, Jung B, Weigang E, Langer M, Hennig J, Frydrychowicz A. Time-resolved 3D MR velocity mapping at 3T: Improved navigator-gated assessment of vascular anatomy and blood flow. J Magn Reson Imaging. 2007;25:824-831